Journal of Alloys and Compounds 1010 (2025) 177017

Contents lists available at ScienceDirect

Journal of Alloys and Compounds

journal homepage: www.elsevier.com/locate/jalcom

Biphasic lithium iron oxide nanocomposites for enhancement in electromagnetic interference shielding properties

Sagnik Ghosh [a], Pramod Rangaiah [b], Mustafa Aboulsaad [a], Sawssen Slimani [c,d], Johan Cedervall [e], Bagher Aslibeiki [f,a], Robin Augustine [b], Tomas Edvinsson [a], Gianni Barucca [g], Davide Peddis [c,d], Tapati Sarkar [a,*]

[a] Department of Materials Science and Engineering, Uppsala University, Box 35, Uppsala SE-75103, Sweden
[b] Department of Electrical Engineering, Solid-State Electronics, Uppsala University, Box 65, Uppsala SE-751 03, Sweden
[c] Dipartimento Di Chimica E Chimica Industriale & INSTM RU, nM2-Lab, Università degli Studi di Genova, Via Dodecaneso 31, Genoa 1-16146, Italy
[d] CNR, Istituto di Struttura della Materia, nM2-Lab, Monterotondo Scalo, Roma 00015, Italy
[e] Department of Chemistry - Ångström Laboratory, Inorganic Chemistry, Box 538, Uppsala SE-751 21, Sweden
[f] Faculty of Physics, University of Tabriz, Tabriz, Iran
[g] Department of Science and Engineering of Matter, Environment and Urban Planning, University Politecnica delle Marche, Via Brecce Bianche 12, Ancona 60131, Italy

ARTICLE INFO

Keywords:
Electromagnetic interference shielding
Nanocomposites
Correlated electron oxide systems
Ferrites
Magnetic properties
Dielectric properties

ABSTRACT

There is a great demand for efficient electromagnetic interference (EMI) shielding materials due to exponential growth in wireless telecommunication devices. These devices emit electromagnetic radiation that can disrupt electronic devices, and cause health hazards. Therefore, it is crucial to develop materials that can shield devices and humans from exposure to electromagnetic radiation. In this context, nanocomposite materials offer huge advantages due to the dual possibility of tailoring the interfaces as well as using the complementary properties of magnetic and dielectric components in the nanocomposite to enhance the EMI shielding performance. This work shows that by a careful tuning of the synthesis parameters, we can grow biphasic lithium iron oxide (ferrimagnetic α-$LiFe_5O_8$ and paramagnetic α-$LiFeO_2$) nanocomposite with different relative fractions of the two phases. The variation of the phase fraction and the simultaneous growth of the two phases allow us to control the interfaces between the two phases as well as the physical properties of the nanocomposite, which have a direct effect on the EMI shielding performance. Detailed structural (X-ray diffraction), compositional (Raman spectroscopy), and morphological (high-resolution transmission electron microscopy) characterization is presented to understand the effect of the synthesis conditions on the EMI shielding parameters. Improved dielectric and magnetic properties together with an increased number of interfaces in the sample with nearly equal amounts of the two phases results in the best performance. This work demonstrates the significant potential of using biphasic magnetic oxide nanocomposites with controllable interfaces and physical properties for EMI shielding, which can form the base for more complex triphasic systems in the future.

1. Introduction

In the current age of technology and wireless communication, electromagnetic interference (EMI) is a major concern in aviation, healthcare, and electronic information systems [1–5]. Nowadays, most devices like smartphones, smart-watches, and computers operate in the microwave frequency region (~10^9 Hz). The exponential proliferation of such wireless devices has led to band congestion [5,6]. EMI occurs when stray microwave frequency signals interfere with electrical devices and cause device malfunction, data corruption, and performance loss. Military aircrafts and equipment like radars also emit electromagnetic (EM) waves that can disrupt other electrical instruments and even pose health threats to plants, animals, and humans [1–8]. To combat these serious challenges, research on EMI-shielding materials has gained increased attention in the last few years. An EMI-shielding material 'shields' the device by blocking unwanted EM waves. The shielding mechanism can be achieved in two ways: reflection of the incident EM waves at the interface, and/or absorption of the EM energy within the material.

* Corresponding author.
E-mail addresses: sagnik.ghosh@angstrom.uu.se (S. Ghosh), tapati.sarkar@angstrom.uu.se (T. Sarkar).

https://doi.org/10.1016/j.jallcom.2024.177017
Received 23 July 2024; Received in revised form 23 September 2024; Accepted 11 October 2024
Available online 13 October 2024

Reflection can be achieved by using highly conductive materials which have free charge carriers that can interact with the incident EM field. Absorption requires the presence of electrical and magnetic dipoles within the material that can dissipate the EM energy in the form of dielectric and magnetic losses [9]. Current research is focused on lightweight EMI-shielding materials that can be effectively integrated into delicate electronic systems, aircrafts, and military gears [10,11].

Metals are highly conductive, and their low skin depth makes them good reflectors of EM waves. However, metals are heavy, and also vulnerable to oxidation and corrosion. Other lightweight candidates include polymer composites that are flexible and resistant to corrosion. However, the degradation of polymers at moderately high temperatures limits their scope in EMI shielding applications [12,13]. Magnetic nanoparticles containing iron have also attracted attention due to their low-cost synthesis, high magnetization, good temperature stability, and better biodegradability [14]. The most important Fe-based compounds include Fe_2O_3 (α, β, γ, and ε polymorphs) [15], ferrites (spinel and hexagonal) [16,17], magnetite (Fe_3O_4) [18], and $LiFeO_2$ (α, β, and γ polymorphs) [19]. These magnetic nanoparticles are often used to make composites with polymers to enhance EMI shielding. Research on multi-component materials involving ferrites, polymers, carbon, and two-dimensional materials is increasing. In multi-component materials, the EMI shielding properties are enhanced due to a synergistic effect and contributions from dielectric and magnetic components. In addition, the increased effect of interfaces between different components in nanocomposites also lead to interfacial polarization effects that can improve absorption of EM waves [20,21]. Microwave absorption properties of α-Fe_2O_3-based composites with interesting morphologies have been investigated thoroughly. Wan et al. devised a novel cellulose-based carbon aerogel/α-Fe_2O_3/polypyrroles composite which registered total shielding effectiveness of 39.4 dB [22]. Manjappa et al. synthesized α-Fe_2O_3/Multi Walled Carbon Nanotube (MWCNT)/graphene nanopellets in low-density polyethylene polymer matrix. The composite with 5 wt% α-Fe_2O_3 exhibited the highest shielding effectiveness (39.19 dB at 10.3 GHz) [23]. Ferrites also enjoy a similar popularity as EMI shielding materials. Lithium ferrite ($LiFe_5O_8$) is one of the most common spinel ferrites used in EMI applications due to its low weight, thermal stability, low-cost synthesis process, and high magnetization [21]. Li et al. fabricated MoS_2/$LiFe_5O_8$ composites with an interesting morphology where raspberry like ferrite particles were lodged on MoS_2 nanoflowers [20]. Lin et al. prepared reduced graphene oxide (r-GO)/ $LiFe_5O_8$ nanocomposites which showed broadband (3.5 GHz) microwave absorption in X-band (8.2 – 12.4 GHz) and Ku-band (12 – 18 GHz) [21]. In both scenarios, the multi-phase composites showed significant enhancement in EMI shielding compared to the individual phases.

Nanostructured $LiFe_5O_8$ can be synthesized using different methods such as sol-gel auto combustion, solid state reaction, and hydrothermal synthesis [24–26]. The sol-gel method is preferred due to the low temperature requirement and greater control over homogeneity and particle size distribution of spinel ferrites [27,28]. Teixeira et al. synthesized $LiFe_5O_8$ using nitrate precursors ($Fe(NO_3)_3{\cdot}9\ H_2O$, and $LiNO_3$) via solid state method and found α-Fe_2O_3 impurity in the samples annealed at 600°C and 1000°C [25]. Lucas et al. encountered α-Fe_2O_3 impurity in lithium ferrite prepared by pectin sol-gel route [24]. This suggests a phase competition, leading to an additional level of complexity in preparing pure $LiFe_5O_8$. Recently, Granados-Miralles et al. explored the effect of Li-content on the phase composition of lithium ferrite. They demonstrated that by increasing the Li:Fe molar ratio to 1:3, a controlled mixture of α-$LiFe_5O_8$ and α-$LiFeO_2$ can be obtained [29]. The tailoring of Li-content is crucial for lithium ferrites as Li tends to evaporate at high processing temperatures. Moreover, the Li-content and the phase composition have significant effect on several physical properties. Sun et al. developed $LiFeO_2$ (13.6 wt%)/$ZnFe_2O_4$(86.4 wt%) composites via sol-gel route. The composites showed significant improvement in dielectric and magnetic properties with minimum absorption loss of −10.4 dB at 17.7 GHz for a thickness of 16.7 mm. The improved absorption was attributed to interfacial polarization loss due to formation of interfaces between $ZnFe_2O_4$ and $LiFeO_2$ [19]. In this context, the possibility to create biphasic lithium ferrite nanocomposite (by changing the initial Li:Fe molar ratio) and thereby increase the number of interfaces offers a way to tune the EMI shielding properties without incorporating a third cation like Zn.

Most reported composite-based EMI shields use several components like MXenes/PBO (poly(p-phenylene-2,6-benzobisoxazole)) nanofiber films[30], liquid metal reinforced cellulose nanofiber/MXene[31], and MXene/polyimide[32] to achieve high shielding effectiveness. These materials typically involve a mixture of two-dimensional materials, polymers, and nanofibers. The formation of multiple hetero-interfaces between different phases has also been exploited to improve microwave absorption[33]. However, the synthesis process of these materials can be complex, time consuming, and expensive. On the other hand, this paper focuses on ceramic materials (i.e., lithium ferrite) that can be easily synthesized using sol-gel auto combustion techniques. A biphasic composite can also be achieved easily by carefully tuning the ratio of the nitrate precursors. Furthermore, since $LiFe_5O_8$ is the preferred choice as the ferrite component in various composite systems for EMI shielding applications, it is interesting to explore the effect of phase competition and varying content of lithium iron oxide phases on its EMI shielding properties. By investigating the effect of Li-content on the EMI shielding properties of lithium iron oxide nanocomposites, we can identify the optimum ratio that will give maximum EMI shielding.

In this framework, lithium-iron oxides with different Li/Fe molar ratios were prepared via the sol-gel route. This paper focuses on the investigation of the synergistic effect of α-$LiFe_5O_8$/α-$LiFeO_2$ on the EMI shielding properties in X-band.

2. Experimental details

Sample Preparation: The lithium-iron oxide nanocomposite samples were synthesized using sol-gel auto combustion method with citric acid as fuel. All chemicals were obtained from Merck and used without further purification. In a typical synthesis, stoichiometric amounts of lithium nitrate ($LiNO_3$), iron (III) nitrate nonahydrate ($Fe(NO_3)_3{\cdot}9\ H_2O$), and citric acid ($HOC(COOH)(CH_2COOH)_2$) were dissolved in de-ionized water. A 1:1 molar ratio of metal nitrates to citric acid was maintained. The water was slowly evaporated by heating at 110°C under continuous magnetic stirring. The resultant viscous gel was heated at 220°C to obtain the final powder product which was thoroughly crushed and annealed at 700°C for 10 h. Four samples were synthesized with different Li/Fe molar ratios of the precursors (Li/Fe = 0, 0.31, 0.50, and 1). The samples are coded as S_1, S_2, S_3, and S_4, respectively **(see** Table 1**)**.

Crystal Structure, Composition, Morphology, and Magnetic Characterization: The crystal structure and phase composition of the annealed powders were investigated using a Siemens D5000 X-ray diffractometer with Bragg-Brentano Focusing Geometry (2θ = 10° to 90°, step size = 0.02°, Cu-Kα radiation with λ = 1.5406 Å) operated at 45 kV and 45 mA. Rietveld refinement was performed on the X-ray diffraction patterns using FullProf suite to reveal the phase composition of the samples [34,35]. During the refinements, several structure parameters were allowed to vary, including the unit cell parameters and atomic positions, and the peak shapes were described using the Thompson-Cox-Hastings pseudo-Voigt function.

The determination of Li and Fe content was carried out by microwave-assisted acid digests. Determination of the elements in the digests was performed by inductively coupled plasma atomic emission spectrometry (ICP-AES) using a Varian Vista PRO instrument. More details of sample preparation for ICP-AES are given in the Supplementary Material. Raman spectra were acquired using a Renishaw inVia Reflex confocal microscope, equipped with a frequency doubled Nd:YAG laser operating at 532 nm with a power of 43 mW for an unmodified laser beam. The single spot and mapping spectra were collected using

Table 1
Table summarizing the sample codes, ratio of nitrate precursors, Li/Fe molar ratio obtained from ICP-AES, and the phase fractions calculated using Rietveld refinement of XRD patterns and Raman mapping. (Errors are shown in parentheses.).

Sample code	Molar ratio of Li/Fe nitrate precursors	Li/Fe molar ratio (from ICP-AES)	Weight percentage of phases from Rietveld refinement (%)			Weight percentage of phases from Raman mapping (%)	
			α - $LiFe_5O_8$	α - $LiFeO_2$	α - Fe_2O_3	α - $LiFe_5O_8$	α - $LiFeO_2$
S_1	-	-	-	-	100	-	-
S_2	0.31	0.30(3)	83.6(5)	16.4(3)	-	84.0(8)	16.0(2)
S_3	0.50	0.44(4)	54.0(3)	46.0(4)	-	55.8(5)	44.2(2)
S_4	1.00	1.0(1)	2.8(8)	97.2(4)	-	-	-

50x objective (Leica), 2400 lines/mm grating, and a laser power adjusted to 5 % of the maximum power (2.15 mW) using neutral density filters to avoid any deterioration from the laser heating. The spectra were recorded with 5–7 seconds acquisition time and 2–3 accumulations, covering a static scan range of 85–1345 cm^{-1}. Prior to spectra acquisition of the samples, the spectrometer was calibrated with measurements on silicon, confirming that the characteristic Si peak is found at 520.5 cm^{-1}.

The inner structure of the samples was investigated by transmission electron microscopy (TEM) techniques. A Philips CM200 electron microscope operating at 200 kV and equipped with a LaB_6 filament was used for the analysis. For TEM observations, the samples in the form of powder were dispersed in ethanol and sonicated for one minute. A drop of the suspension was put over a commercial holed-carbon-coated TEM grid and kept in air until complete ethanol evaporation. Room temperature magnetization hysteresis loops were recorded within a range of −18 kOe to +18 kOe using a vibrating sample magnetometer (LakeShore 7404 VSM).

Microwave Characterization: EMI shielding properties in the X band (8.2 – 12.4 GHz) was studied using a two-port Network Analyzer

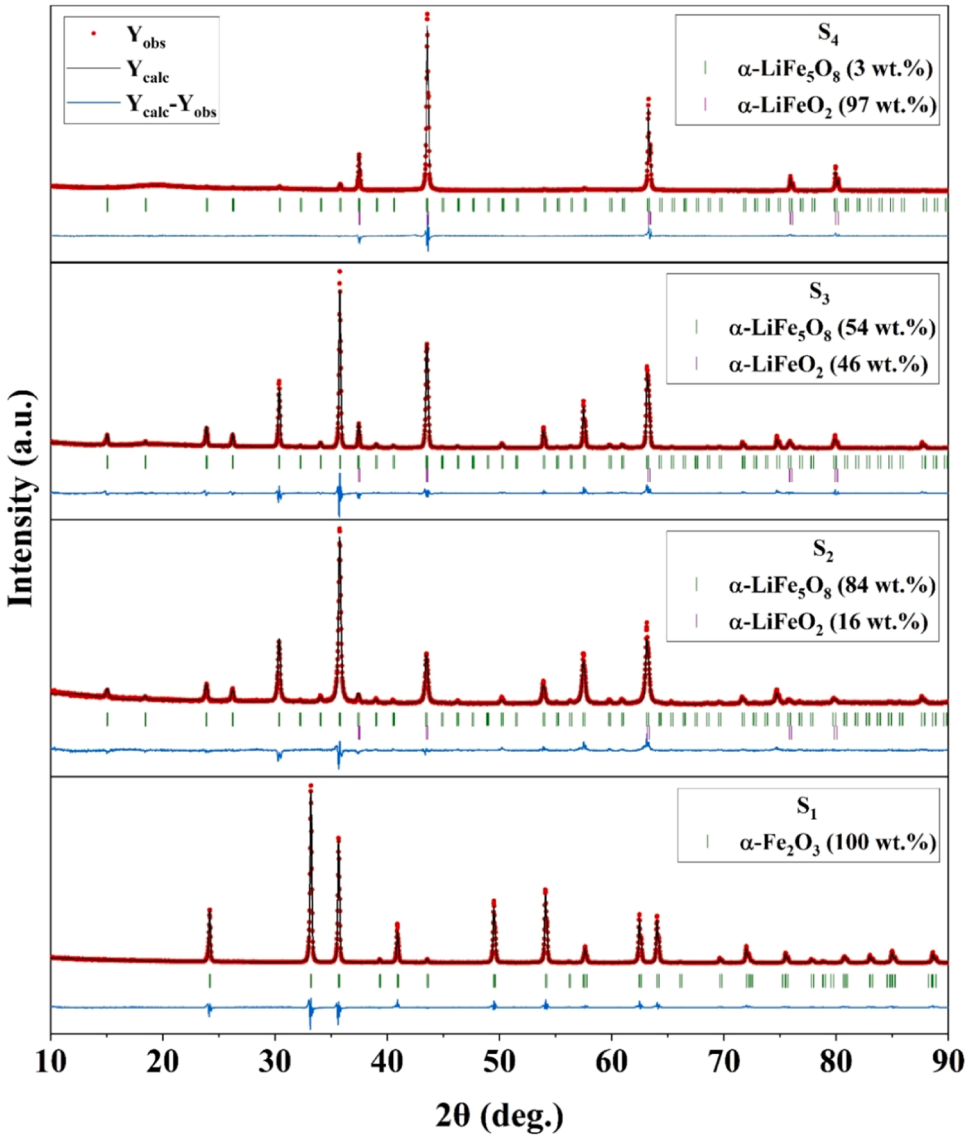

Fig. 1. Rietveld refinement plots of all samples annealed at 700°C.

(Keysight N9918A FieldFox Handheld Microwave Analyser, 26.5 GHz) in Transmission Line mode. The network analyzer was calibrated using the Keysight N9911X-WR90 mechanical calibration kit. A hydraulic press was used to press the powder samples at 30 kN pressure to produce rectangular pellets of required dimensions (22.85 mm × 10.16 mm × 3 mm). The pellets were then tightly fitted into the waveguide to obtain the EMI shielding response. The complex permittivity and permeability values were calculated by the Nicolson – Ross – Weir Method using Keysight N1500A Materials Measurement Suite (2020).

In Fig. S1 in the Supplementary Material, a schematic diagram shows the full sample preparation flow, starting from the precursors to the final pellet used for the microwave characterization.

3. Results and discussion

3.1. Structural characterization and phase composition

X-ray diffraction (XRD) patterns (Fig. S2 **in the** Supplementary Material) were recorded to reveal the mono/biphasic nature of the samples formed as a result of varying the initial Li:Fe molar ratio in the nitrate precursors. The XRD pattern for sample S_1 (Li/Fe = 0) matched with the standard pattern of α-Fe_2O_3 ($R\bar{3}c$) indicating that the absence of Li results in the formation of pure α-Fe_2O_3. The XRD patterns of S_2, S_3, and S_4 showed coexistence of α-$LiFe_5O_8$ ($P4_332$) and α-$LiFeO_2$ ($Fm\bar{3}m$). A molar ratio of Li/Fe = 0.2 is expected to yield single-phase α-$LiFe_5O_8$ [25,29]. To form biphasic lithium iron oxide, we have intentionally selected initial molar ratios of Li/Fe > 0.2 during synthesis for samples S_2, S_3, and S_4. This leads to the formation of the secondary phase of α-$LiFeO_2$, as has been reported in literature [29]. S_4 has a molar ratio of Li/Fe = 1, which leads to the formation of α-$LiFeO_2$ majority phase, while the α-$LiFe_5O_8$ phase is significantly suppressed. The obtained diffraction patterns were analyzed using the Rietveld method implemented in the software FullProf. The XRD patterns were analysed, and the refinements are shown in Fig. 1. S_2, S_3, and S_4 were analysed using a biphasic refinement using the phases α-$LiFe_5O_8$ and α-$LiFeO_2$, whereas S_1 could be indexed with the single-phase α-Fe_2O_3. The phase fractions obtained from the refinements are summarised in Table 1. These indicate that increasing the initial Li/Fe molar ratio increases the amount of α-$LiFeO_2$ phase in the final sample. During the refinements, the Fe/Li occupancies within the α-$LiFe_5O_8$ phase were also refined, but no systematic changes were seen in the calculated diffraction pattern nor were there any systematic changes between the different samples. The refined unit cell parameters are presented in Table 2 and are in good agreement with reported works [29,36].

Raman mapping of the samples were performed to further check the phase quantification as an additional confirmation of the phase fractions obtained from XRD. The Raman spectra of the samples are depicted in Fig. 2. For sample S_1, the obtained Raman spectrum (shown in Fig. 2a) has all the characteristic peaks corresponding to the α-Fe_2O_3 phase. The peaks located at 224 and 498 cm^{-1} are assigned to the A_{1g} modes while the remaining peaks at about 244, 291, 408, 609, and 818 cm^{-1} correspond to the E_g modes [37–39]. The peaks around 1056 and 1315 cm^{-1} are also associated with α-Fe_2O_3 [38]. No other significant peaks are present in the spectrum which reinforces the X-ray diffraction analysis and confirms the formation of pure hematite (α-Fe_2O_3) phase.

For samples S_2 and S_3, Raman scans at different parts of the sample yielded different spectra, which were a combination of the spectra of the two phases α-$LiFe_5O_8$ (Fig. 2b) and α-$LiFeO_2$ (Fig. 2c). In Fig. 2b, the Raman modes of the $LiFe_5O_8$ spinel phase are observed with the peaks around 199 cm^{-1} and 235 cm^{-1} confirming the presence of the α-phase. $6A_1 + 14E + 20\ F_2$ Raman modes are allowed for the α-polymorph of the $LiFe_5O_8$ phase [25,29,40,41]. The most prominent Raman peaks are observed around 126, 199, 235, 261, 298, 353, 378, 396, 439, 488, 603, and 707 cm^{-1}. The band located near 1160 cm^{-1} corresponds to second-order mode [29]. In Fig. 2c, the obtained spectrum from S_4 is completely different from that of the $LiFe_5O_8$ spinel phase. Three main broad peaks are present roughly around 180, 394, and 624 cm^{-1} which correspond to the $LiFeO_2$ phase with rock salt structure. $A_1 + E_g$ are the Raman active modes in $LiMO_2$ (M = Ni, Co, Cr) type materials. Apart from the broad peaks, a second order mode is also present at 1256 cm^{-1} [29,42]. S_4 exhibits only the α-$LiFeO_2$ spectrum since $LiFeO_2$ is the majority phase in S_4 as per XRD data. Fig. 2d depicts a mixed Raman spectrum obtained from S_3 which exhibits contribution from both α-$LiFe_5O_8$ and α-$LiFeO_2$ phases. It is evident that Fig. 2d is a superposition of Figs. 2b and 2c. To quantify the phase fraction of S_2 and S_3, Raman mapping was performed on both samples with a spot size of 1 μm to ensure better spatial resolution. The phase fractions obtained from the mapping data are in good agreement with those obtained from X-ray diffraction data (Table 1). Similar Raman mapping technique has been used in literature to quantify the $LiFeO_2$ secondary phase in $LiFe_5O_8$ [29]. Details of the mapping spectra and the method of phase fraction calculation are described in the supplementary material (Figs. S3 and S4 in the Supplementary material).

Table 2
Refined unit cell parameters of the samples. (Errors are shown in parentheses.).

Sample code	Unit cell parameters (Å)			
	$LiFe_5O_8$ – (*a*)	$LiFeO_2$ – (*a*)	Fe_2O_3 – (*a*)	Fe_2O_3 – (*c*)
S_1	-	-	5.0334(2)	13.7436(6)
S_2	8.3274(5)	4.1590(5)	-	-
S_3	8.3238(3)	4.1566(2)	-	-
S_4	8.316(1)	4.1535(1)	-	-

3.2. Inner structure – morphology and interfaces

S_2 and S_3, the two samples with appreciable amounts of the two phases, were selected for TEM analysis to further investigate the structure and morphology of the materials (Fig. 3). In particular, Fig. 3a shows a typical bright field image of the S_2 sample which appears composed of large aggregates of grains having a regular shape. The corresponding selected area electron diffraction (SAED) pattern is imaged in the inset and all the visible diffraction spots can be attributed to the α-$LiFe_5O_8$ phase. The S_2 sample is composed mainly of the α-$LiFe_5O_8$ phase, as indicated by XRD measurements (approximately 84 %), so the sample morphology can be attributed to the α-$LiFe_5O_8$ phase. Bright-field TEM images of the S_3 sample are shown in Fig. 3b-d. This sample is composed of large grains' aggregates as S_2, but only a few regions show grains with a regular shape (Fig. 3c), while a major part of the sample reveals the presence of grains having an irregular, pointed shape (Figs. 3b and 3d). The SAED pattern of the sample's area of Fig. 3d is shown in Fig. 3e. Although it is difficult to distinguish among the interplanar distances of the α-$LiFeO_2$ and α-$LiFe_5O_8$ phases, the diffraction spots corresponding to the interplanar distance d = 0.239 nm can be presumably attributed to the {111} atomic planes of α-$LiFeO_2$ rather than the {222} planes of α-$LiFe_5O_8$ because the intensity for these spots should be 5/100 of the intensity of the spots corresponding to d (311) = 0.251 nm for the α-$LiFe_5O_8$ phase. In this case, the intensity between the diffraction spots is approximately the same (see magnified area of Fig. 3e) suggesting the presence of the α-$LiFeO_2$ phase, in addition to the α-$LiFe_5O_8$ phase to which some diffraction points can be uniquely attributed. In any case, XRD measurements and Raman mapping indicate the presence of ~45 % of α-$LiFeO_2$ in the S_3 sample and TEM analysis reveals that the simultaneous growth of the two phases tends to modify the growth of the α-$LiFe_5O_8$ grains. They appear more irregular suggesting an increase in interfaces with other grains. Due to the very similar lattice parameters, a more careful investigation of the interface appears to be tricky. Moreover, elemental analysis using energy dispersive spectroscopy (EDS) is also not straightforward in these samples. More details on these limitations are provided in section 1.5 of the Supplementary Material.

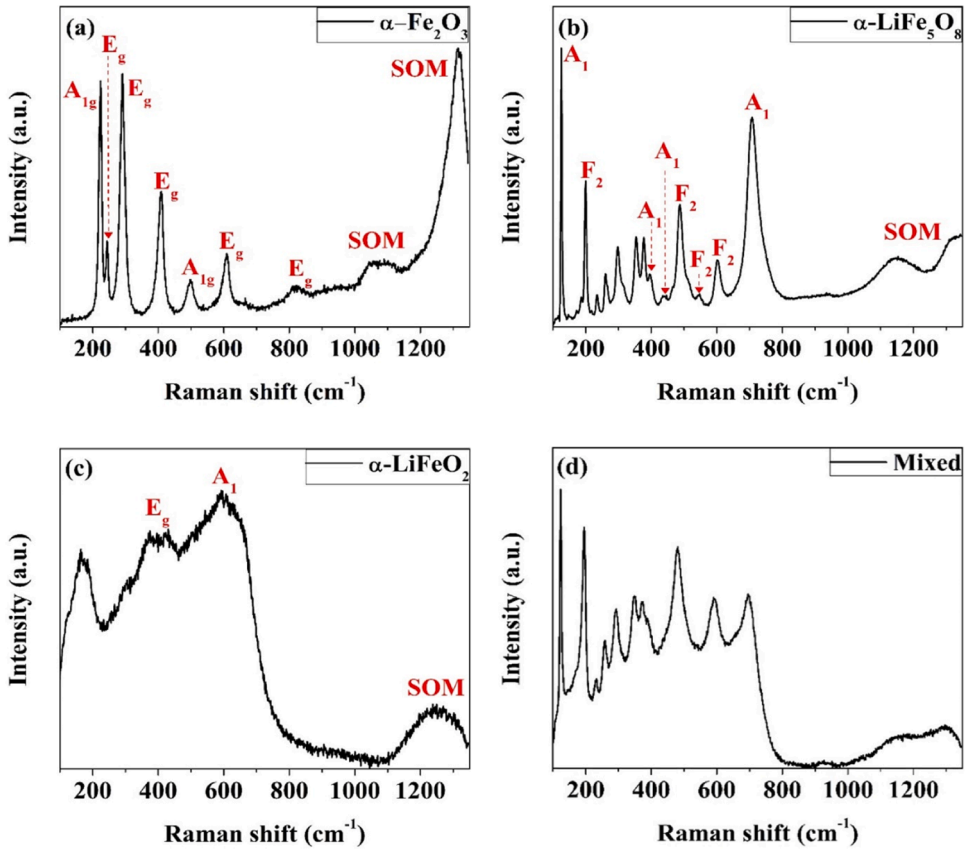

Fig. 2. Raman spectra of (a) α-Fe_2O_3 obtained from S_1, (b) α-$LiFe_5O_8$, (c) α-$LiFeO_2$, and (d) mixed spectrum from S_3 exhibiting signals from both α-$LiFe_5O_8$ and α-$LiFeO_2$ phases under 532 nm laser illumination. SOM indicates second order modes.

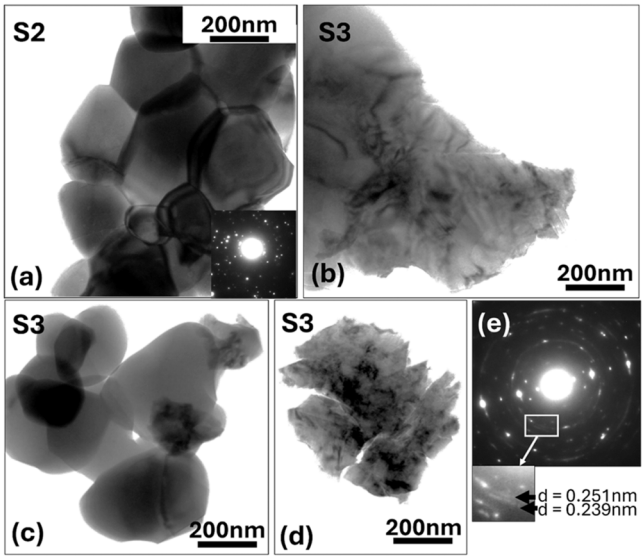

Fig. 3. Bright-field TEM images of (a) S_2 and corresponding SAED pattern (inset), (b-d) S_3 showing different grains' morphology. (e) SAED pattern of the grains shown in (d); magnified area evidence portions of the diffraction rings that can be attributed to α-$LiFe_5O_8$ (d = 0.251 nm) and α-$LiFeO_2$ (d = 0.239 nm).

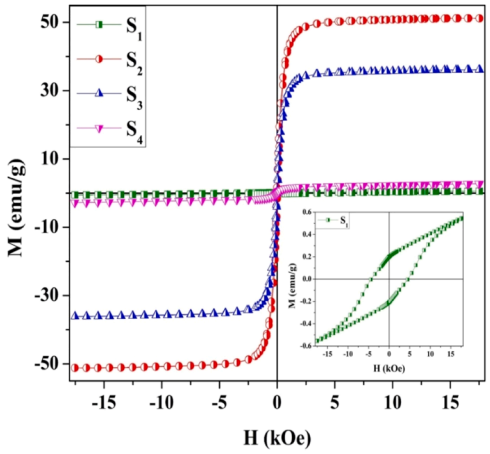

Fig. 4. Field dependence of magnetization at 300 K. Inset: Enlarged portion of the M-H loop of S_1 around the origin.

3.3. Magnetic properties

The M-H loops recorded at 300 K (Fig. 4) show lower saturation magnetization (M_S) for samples with lower fraction of α-$LiFe_5O_8$ following closely the trend obtained from Rietveld refinement (Table 1). S_1 is composed of pure α-Fe_2O_3 phase which exhibits weak ferromagnetic behavior characterised by a wide M-H loop with magnetization of 0.55 emu/g at 17.55 kOe, coercivity (H_C) of ~4390 Oe, and remanent magnetization (M_r) of 0.20 emu/g, all of which are in good agreement with other reports in literature. Coercivity and other magnetic properties of α-Fe_2O_3 are greatly influenced by temperature, morphology, and factors like shape anisotropy [43–45]. The unusual hysteresis behavior of α-Fe_2O_3 has been attributed to its antiferromagnetic core which is represented by the absence of saturation and linear dependence of the M-H curve at higher magnetic fields. The surface spin disorder may be

responsible for the weak ferromagnetism and large hysteresis. [44,46]. Both S_2 and S_3 have large amount of the soft ferrimagnetic $LiFe_5O_8$ phase which results in high saturation magnetization and low coercivity. In spinel-ferrites like α-$LiFe_5O_8$, the magnetization behavior is determined by the cationic distribution in A (tetrahedral) and B (octahedral) sites as per Néel's sublattice model. According to the sublattice model, the magnetic response is due to the contribution from AB sites and not due to the interactions from AA and BB sites. The resultant magnetization is obtained from the difference of the A and B sub-lattice magnetizations [47]. In the ordered α-$LiFe_5O_8$, the octahedral *4b* sites are occupied by the Li^{+} cations while iron (Fe^{3+}) cations occupy the tetrahedral *8c* (A site) and octahedral *12d* (B site) positions [48–50]. S_2, which has ~84 wt% α-$LiFe_5O_8$ phase exhibited a saturation magnetization of 52 emu/g. In literature, it is reported that pure α-$LiFe_5O_8$ has a slightly higher saturation of approximately 61.5 – 64.4 emu/g [29,36]. Therefore, the lower saturation value obtained in this work can be attributed to the presence of the paramagnetic α-$LiFeO_2$ phase (~16 wt% as per Rietveld analysis), which has an antiferromagnetic ordering temperature far below room temperature [29]. In S_3, the weight fraction α-$LiFeO_2$ is much higher (~46 wt% as per Rietveld analysis) which further reduces the saturation magnetization (36 emu/g). In fact, considering that 100 wt% α-$LiFe_5O_8$ exhibits an M_S value of 61.5 emu/g, ~84 wt% α-$LiFe_5O_8$ (in S_2) and ~54 wt% α-$LiFe_5O_8$ (in S_3) should exhibit M_S values of 51.66 emu/g and 33.21 emu/g respectively, which are remarkably close to the observed value of M_S in the two samples. Finally, in S_4, α-$LiFeO_2$ is the majority phase (~97 wt%) along with a small amount of α-$LiFe_5O_8$ (~3 wt%). In literature, the room temperature magnetization curve of pure α-$LiFeO_2$ exhibits a linear paramagnetic behavior with a magnetization of 1 emu/g at 20 kOe [42]. This explains the low magnetization and linear behavior of the M-H curve along with a small amount of hysteresis arising from the presence of α-$LiFe_5O_8$. However, sample S_4 has a slightly higher coercivity (80 Oe) than S_2 and S_3 (< 50 Oe). The increase in coercivity can be due to the dispersion of small amounts of ferrimagnetic α-$LiFe_5O_8$ in a nonmagnetic $LiFeO_2$ matrix which reduces dipole-dipole interactions and increases magnetic hardening [29,51,52]. Apart from the phase fractions and cationic distribution, the magnetic properties can also be influenced by homogeneity, defects, porosity, grain size, and synthesis conditions. The obtained magnetic parameters are listed in Table 3. The step size of the applied field (H) was 50 Oe and hence coercivity values less than 50 Oe fall below the tolerance limit of the measurement.

3.4. EMI shielding performance

The EMI shielding performance of a material is measured by its ability to attenuate and dissipate the incident electromagnetic (EM) wave and 'shield' the enclosed device. When an EM wave is incident on a dielectric medium, a fraction of the incoming power is reflected while another part is absorbed within the medium. The remaining part is transmitted across the dielectric. Due to the law of conservation of energy, the power coefficients corresponding to transmission (T), absorption (A), and reflection (R) must add up to unity ($R + A + T = 1$) [53,54]. According to the calculation theory of shielding effectiveness [53], the total shielding effectiveness (SE_T) of a shielding layer can therefore be expressed as a ratio of the transmitted power (P_{out}) to the incident power (P_{in}).

Table 3
Saturation magnetization (M_S), coercivity (H_C), and remanence magnetization (M_r) of the samples at 300 K. (Errors are shown in parentheses.).

Sample	M_S (emu/g)	H_C (Oe)	M_r (emu/g)
S_1	0.55(3)	4390	0.20(1)
S_2	52(3)	< 50	4.1(2)
S_3	36(2)	< 50	1.9(1)
S_4	2.8(1)	80	0.27(1)

$$SE_T(dB) = 10\log_{10}\left(\frac{P_{in}}{P_{out}}\right) = 10\log_{10}\left|\frac{1}{T}\right| = SE_R(dB) + SE_A(dB) \quad (1)$$

Here, SE_R represents the loss in power due to reflection. Reflection occurs at the interface between two media when there is an impedance mismatch. When the impedance mismatch is large, the reflection is also large. The electromagnetic impedance faced by an EM wave travelling through any material medium is given by the ratio of the electric and magnetic fields. Air has an impedance of approximately 377 Ω while ferrites have much lower impedance causing a large impedance mismatch at the air-ferrite interface. This results in large reflection of the EM wave. The reflection loss due to shielding (SE_R) [53] can be expressed as,

$$SE_R(dB) = 10\log_{10}\left|\frac{1}{1-R}\right| \quad (2)$$

The power that enters the material is partly absorbed while the rest is transmitted. SE_A denotes the shielding due to absorption [53] and is expressed as,

$$SE_A(dB) = 10\log_{10}\left|\frac{1-R}{T}\right| \quad (3)$$

SE_A quantifies the ability of the material to absorb the EM wave that has penetrated the material. When there is good impedance matching at the interface, EM waves suffer negligible reflection and penetrate the material. In such cases, absorption becomes the dominant shielding mechanism. The contribution of absorption in the shielding mechanism can be estimated by the absorption efficiency (A_{eff} %) [50] given as,

$$A_{eff}(\%) = \frac{(1-R-T)}{(1-R)} \times 100 \quad (4)$$

For example, an A_{eff} of 50 % means that 50 % of the power that penetrated the material was absorbed. The total EMI shielding effectiveness (SE_T) in dB can also be expressed as EMI shielding efficiency (SE_{eff} %), which denotes the total percentage of power blocked by the shielding layer.

$$SE_{eff} \quad (\%) = 100 - \left(\frac{1}{10^{\frac{SE_T}{10}}}\right) \times 100 \quad (5)$$

The shielding effectiveness of a material is greatly influenced by its dielectric and magnetic properties. As per the EM theory, *ac* conductivity ($\sigma_{ac} = \omega\varepsilon_0\varepsilon''$, where ω is the angular frequency of incident EM wave, ε_0 is the permittivity of free space, and ε'' is the imaginary part of complex permittivity), permeability (μ_r), and thickness (d) of the medium defines the total shielding effectiveness of the medium [50,55] as follows:

$$SE_T(dB) = SE_R(dB) + SE_A(dB) \approx 10\log_{10}\left(\frac{\sigma_{ac}}{16\omega\varepsilon_0\mu_r}\right) + 20d\sqrt{\frac{\mu_r\omega\sigma_{ac}}{2}}\log_{10}e \quad (6)$$

SE_R therefore increases with an increase in ac conductivity (σ_{ac}) but decreases when the frequency (ω) and permeability (μ_r) of the shielding medium increase. The shielding performance of a material can thus be improved by carefully tuning its magnetic and dielectric properties. In this work, the reflection (R) and transmission (T) coefficients were calculated from the measured S-parameters [53].

The SE_R, SE_A, and SE_T values of all samples are plotted as a function of frequency (in the X-band) in Fig. 5. The SE_R values of all samples lie within a range of 6.2 – 3.6 dB, while the SE_A values vary between 3.8 – 0.1 dB. The higher value of SE_R indicates that reflection is the dominant shielding mechanism throughout the X-band. S_4 exhibits the highest SE_R value below 9.4 GHz suggesting that α-$LiFeO_2$ offers significant impedance mismatch at the interface causing high reflection. From

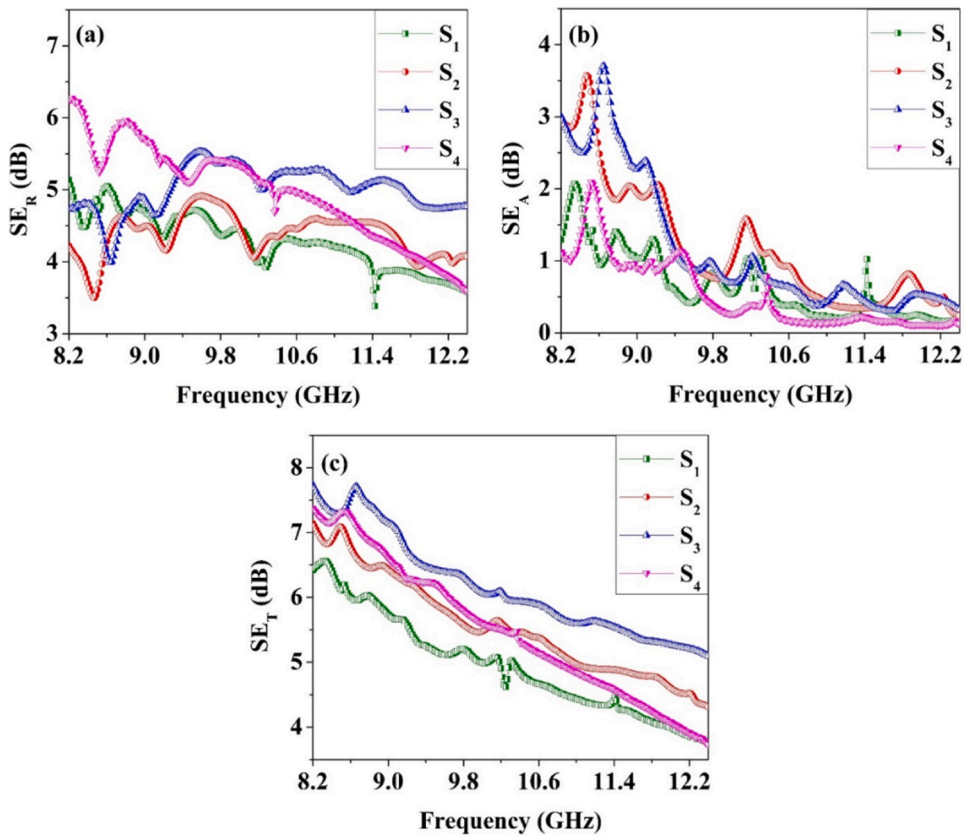

Fig. 5. EMI shielding effectiveness of all samples as a function of frequency. (a) SE_R, (b) SE_A, and (c) SE_T.

~10.3 GHz, sample S_3 exhibits the highest SE_R value while the other samples have lower reflection losses at higher frequencies. For SE_A, both S_2 and S_3 exhibit comparable values throughout the X-band. S_2 and S_3 have large amounts of ferrimagnetic α-$LiFe_5O_8$ phase, resulting in higher absorption due to higher magnetic loss. For losses within the material, magnetic and electric dipoles must be present. Therefore, lower absorption losses in S_1 and S_4 may be due to the absence of the ferrimagnetic phase [9,56]. By comparing the SE_R and SE_A data, it is observed that in S_1 (100 wt% α-Fe_2O_3) and S_4 (97.2 wt% α-$LiFeO_2$), the shielding mechanism is completely dominated by reflection. Therefore, both α-Fe_2O_3 and α-$LiFeO_2$ are poor absorbers in the X-band. Both SE_R and SE_A are affected by conductivity and permeability, which suggests that the co-existence of almost equal amounts of two phases in S_3 (54 wt% ferrimagnetic $LiFe_5O_8$, 46 wt% paramagnetic $LiFeO_2$) may have resulted in improved dielectric and magnetic properties. It has been reported in literature that the presence of $LiFeO_2$ secondary phase can effectively modify the dielectric and magnetic parameters of $ZnFe_2O_4$ [19]. Interestingly, calculating SE_T (shown in Fig. 5c), which is an additive combination of SE_R and SE_A, we find that S_3 (the biphasic sample with nearly equal amounts of the two phases) exhibits the highest total shielding effectiveness (SE_T) throughout the X-band, while S_1 (the only completely single-phase sample) shows the poorest performance. This indicates the advantage of using biphasic samples with increased number of interfaces over pure single phases for achieving better total shielding performance.

Shielding efficiency (%) and absorption efficiency (%) were calculated (Fig. 6a, b) to better understand the shielding performance and mechanism. The shielding efficiency of all samples decreased monotonically with increase in frequency. At 8.2 GHz, S_3 blocks ~83 % of the incoming EM radiation, while S_1 blocks ~77 %. The performance gap increases at higher frequencies with S_3 blocking ~69 % of the incoming radiation at 12.4 GHz compared to only ~58 % by S_1. For most of the X-band, absorption efficiency (A_{eff} %) of all samples is less than 50 %, indicating that the samples are not good absorbers in the measured frequency range. Nevertheless, we note that S_3 exhibited the highest absorption efficiency of ~57 % at ~8.65 GHz, slightly outperforming its nearest competitor S_2 (also a biphasic sample with appreciable amounts of both phases), which registered a maximum A_{eff} of ~56 % at ~8.47 GHz. The synergistic effect of α-$LiFe_5O_8$/α-$LiFeO_2$ has thus modified the EMI shielding parameters, resulting in improved performance of sample S_3. The presence of increased number of interfaces between $LiFeO_2$ and $LiFe_5O_8$ (as indicated by TEM analysis) can cause interfacial polarization increasing the dielectric loss and absorption efficiency [19]. A schematic illustration of the shielding mechanism in biphasic lithium iron oxide is provided in the lower panel of Fig. 6). The important shielding parameters of the samples are tabulated in Table S1 (in the Supplementary Material). We also compare the total shielding effectiveness of similar ferrite-based materials with that of sample S_3 (Table 4). S_3 has better shielding performance than those reported for pure phase iron oxides and oxides like γ-Fe_2O_3, $LiFe_5O_8$, and Mn_3O_4. Moreover, it showed slightly better or similar shielding as obtained for ferrite/polymer and ferrite/two-dimensional composite systems.

The reflection loss (RL) values were also calculated to quantify the microwave absorption capability of the samples. The method of calculation is provided in Section 1.6 in the Supplementary Material. For good microwave absorption performance, RL value of less than −10 dB is desirable[57–60]. The corresponding frequency range is defined as the effective absorption bandwidth (EAB). The frequency variations of RL for different sample thicknesses are provided in Fig. S5 in the Supplementary Material. All the samples show good microwave absorption properties with RL values varying between −10 dB to −30 dB for most of the X-band. At a thickness of 4 mm, the EAB of sample S_1 and S_4 are approximately 2.7 GHz and 2.3 GHz, respectively. The EAB improved with higher $LiFe_5O_8$ content in S_2 and S_3. For S_2, a maximum EAB of 3.6 GHz is observed, whereas, for S_3 the EAB is approximately 3 GHz. The frequency variation of the impedance matching for all samples is shown in Fig. S6 in the Supplementary Material. Overall, the samples

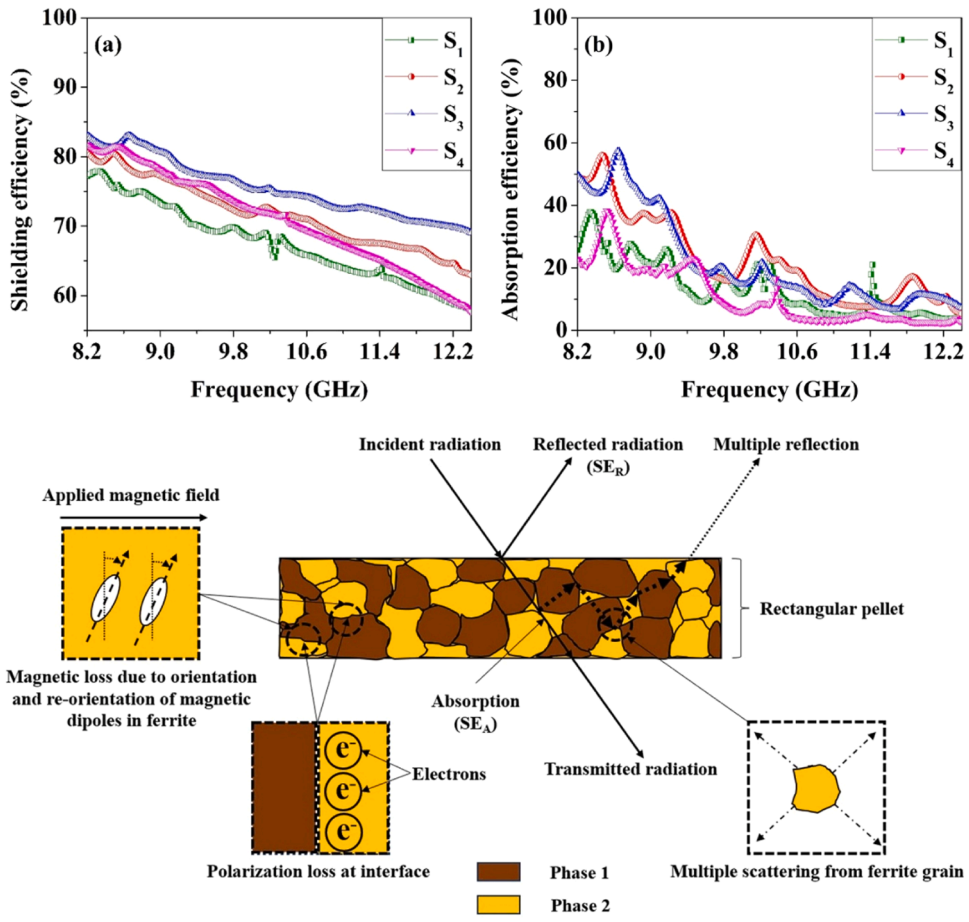

Fig. 6. (a) Shielding efficiency and (b) absorption efficiency as a function of frequency. Lower panel: Schematic illustration of electromagnetic interference shielding mechanism in biphasic lithium iron oxide.

Table 4
Comparison of EMI shielding effectiveness (SE_T) of reported materials with this work.

Material	Frequency (GHz)	SE_T (dB)	Thickness (mm)	Reference
$LiFe_5O_8$	2 – 18	6.27	3	[50]
$LiFe_5O_8$/ Carbon black (5 wt%)	2 – 18	10.42	3	[50]
5 wt% RGO@MoS_2 + PVDF	2 – 18	~ 6	1 – 5	[61]
Mn_3O_4	2 – 18	~ 2.5	-	[62]
MoS_2-RGO/Fe_3O_4	8.2 – 12.4	8.27	-	[63]
γ-Fe_2O_3	8.2 – 12.4	2.5	3	[64]
LDPE:MWCNT:GNP: $ZrFe_2O_4$ (50:5:5:40)	8.2 – 12.4	5.09	3.5	[65]
Graphene/epoxy composite (1 wt% loading)	8.2 – 12.4	< 5	-	[66]
S_3 (54 wt% α-$LiFe_5O_8$/ 46 wt% α-$LiFeO_2$)	8.2 – 12.4	7.74	3	**This work**

with biphasic lithium iron oxide show better microwave absorption properties and wider EABs. Better absorption properties can be attributed to the formation of interfaces among the two competing phases[58,59]. Moreover, $LiFe_5O_8$ is a soft ferrimagnetic material, whereas $LiFeO_2$ has better dielectric property. This can lead to magnetic-dielectric synergy which boosts microwave absorption[58].

3.5. Permittivity and permeability

To understand better the effects of the magnetic and dielectric properties of the composites on the EMI shielding performance, the complex permittivity (ε_r) and permeability (μ_r) values were calculated from the scattering (S) parameters (obtained from the vector network analyzer) using the Nicolson – Ross – Weir algorithm [67]. The obtained results are plotted as a function of frequency in Fig. 7a – d. The relative permittivity of a medium can be expressed as the sum of real and imaginary parts ($\varepsilon_r = \varepsilon' - j\varepsilon''$). The real part of permittivity (ε') gives a measure of the polarization within the material. When EM waves propagate through the material, a part of its energy is dissipated in the form of heat which can be quantified by the imaginary part (ε'') of the complex permittivity. Permittivity of a material is mainly determined by electronic, ionic, dipolar, and interfacial polarization. Electronic and ionic polarization governs the permittivity behavior in the GHz frequency range[56,68,69]. From Fig. 7a, it is evident that the ε' values of the samples do not vary much with increasing frequency. For S_1 containing pure α-Fe_2O_3, ε' ranges from 6 – 6.7. S_2, which has a majority α-$LiFe_5O_8$ phase exhibits ε' value of ~5.5 – 6. This indicates that the soft ferrimagnetic α-$LiFe_5O_8$ phase has lower dielectric polarization. The value of ε' increases with increase in wt% of α-$LiFeO_2$ in the sample and attains a maximum value of ~7.5 – 8.6 for S_4 (~97.2 wt% α-$LiFeO_2$). Thus, the dielectric property of biphasic lithium iron oxide can be tuned by controlling the relative weight percentages of α-$LiFeO_2$ and α-$LiFe_5O_8$. The effective medium theory states that increase in conductivity leads to an increase in ε'. However, very high ε' can generate surface eddy currents which increase reflection of microwave signals at the interface and minimises absorption [70]. Therefore, to obtain good

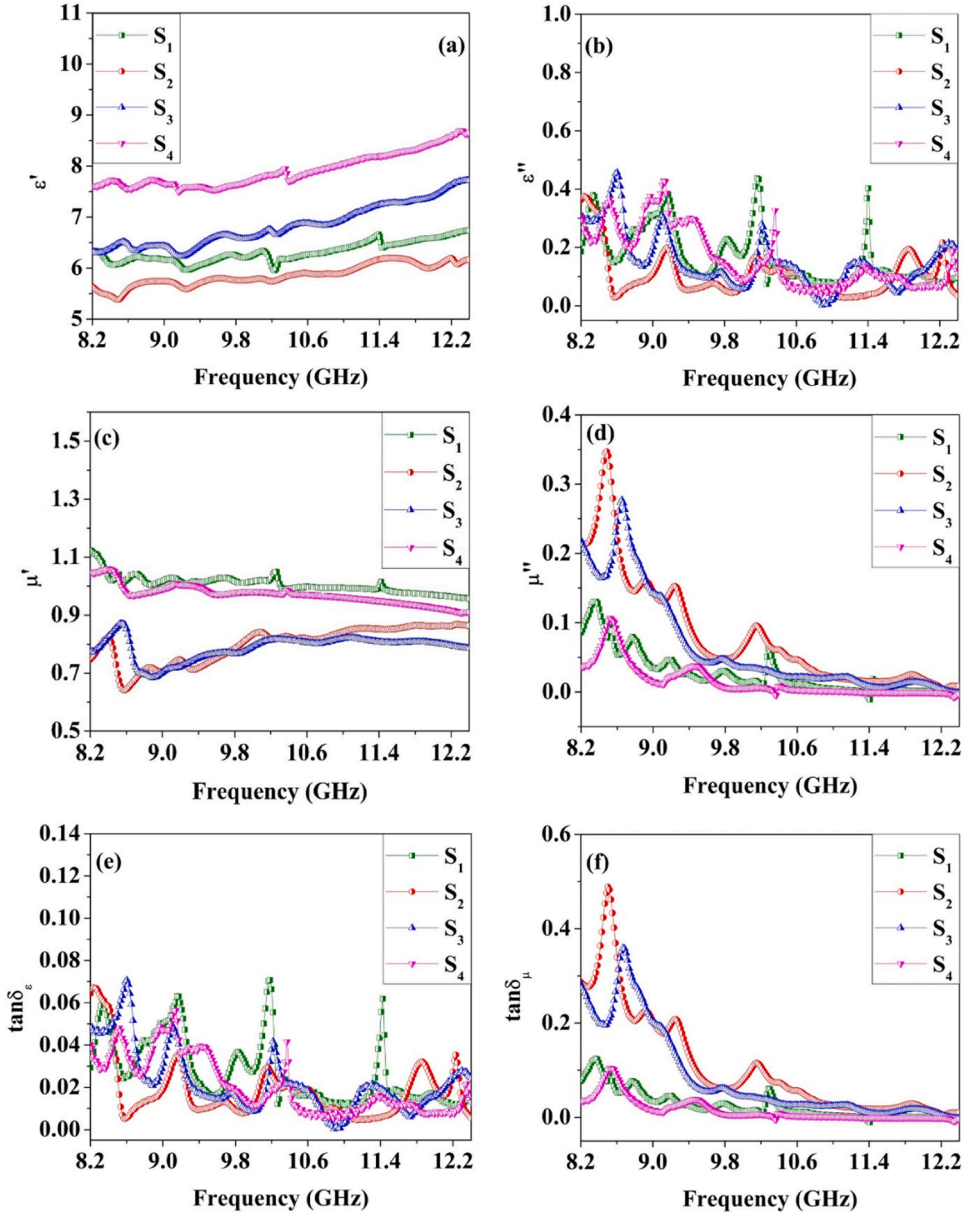

Fig. 7. (a, c) Real and (b, d) Imaginary parts of permittivity (ε_r) and permeability (μ_r) in X-band, (e) Dielectric and (f) magnetic loss tangents as a function of frequency.

impedance matching, the ε' value must be tuned properly. From Fig. 7b, it is clear that all the samples have very similar ε'' values in the X-band. However, a closer look reveals that S_2 has a slightly lower ε'' value compared to the other samples, indicating lower dielectric loss. The dielectric loss tangent ($\tan\delta_\varepsilon = \varepsilon''/\varepsilon'$) represents the dielectric loss suffered by the EM waves that enter the material [70]. The loss tangent, shown in Fig. 7e, has a similar trend to ε''. Loss tangent values of all samples lie within a range of 0.07 – 0.01, indicating that all the samples are low-loss dielectrics. According to Eq. 6, increase in conductivity (σ_{ac}) improves both SE_R and SE_A. Therefore, conductivity plays an important role in shielding. The frequency variation of conductivity of the samples in the X band is depicted in Fig. S7 (in the Supplementary Material). The conductivity of all samples vary within the range of 0.01 – 0.26 S/m.

Complex permeability (μ_r) also has real and imaginary components ($\mu_r = \mu' - j\mu''$). The complex permeability (μ' and μ'') values are plotted in Fig. 7c and d. μ'' denotes the magnetic loss in the material. The real part of permeability (μ') has very small fluctuations throughout the X -band. S_1 has a μ' value close to 1, while the μ'' value varies between 0.1 and 0. This is expected as S_1 (pure α-Fe_2O_3) is antiferromagnetic with very low values of magnetization [71]. A similar trend in μ' and μ'' is observed for S_4, which is reasonable since S_4 has paramagnetic (at room temperature) α-$LiFeO_2$ as the major phase. In contrast, both S_2 and S_3 exhibit higher values of μ'' which correspond to higher magnetic losses due to the presence of the ferrimagnetic α-$LiFe_5O_8$ phase. The magnetic loss in S_2 is slightly higher than that in S_3 due to the presence of greater wt% of α-$LiFe_5O_8$ in S_2. Hysteresis loss is an important mechanism of shielding[72]. When subject to rapid magnetization and demagnetization, the orientation of magnetic dipoles within a material lags behind the applied field. Therefore, the incident magnetic energy gets converted to heat. The permeabilities (μ') of S_1 and S_4 are close to 1 which indicates that they offer less resistance to the incoming magnetic field. Moreover, both have very low saturation magnetization (Fig. 4). Hence, S_1 and S_4 allow the magnetic part of the electromagnetic waves to pass with little attenuation. This is reflected in the lower values of magnetic loss (μ'') for S_1 and S_4 (Fig. 7d). However, the ferrimagnetic samples S_2 and S_3 possess sufficient magnetic dipoles that can interact strongly with

the incoming magnetic fields resulting in hysteresis loss and conversion of magnetic energy into heat. The absorption of magnetic energy and its dissipation as heat is evident from the higher magnetic loss (μ'') for S_2 and S_3.

The magnetic loss tangent ($\tan\delta_\mu = \mu''/\mu'$) of the samples are shown in Fig. 7f. We observe some peaks in the μ'' and $\tan\delta_\mu$ curves within the frequency range 8.2 – 10.6 GHz. Peaks located at these low frequencies are typically attributed to natural ferromagnetic resonance, whereas peaks at very high frequencies correspond to exchange resonance [9]. Magnetic losses in the microwave range, especially in ferrites can be caused either by eddy current loss or due to natural resonance. For magnetic nanoparticles, the eddy current loss is influenced by the electrical conductivity (σ_{ac}) and diameter of the nanoparticle and can be expressed as $C_o = \mu''(\mu')^{-2}f^{-1}$, where, f is the frequency of the microwave signal. As per the skin-effect criterion, if C_o remains constant with varying frequency, then the magnetic loss can be attributed to eddy current loss [9,70,73]. In our case, C_o varies significantly for S_2 and S_3 (Fig. S8 in the Supplementary Material), which indicates that the peaks in the frequency range 8.2 – 10.6 GHz do not originate from eddy current loss but can instead be attributed to natural resonance [70]. The permittivity and permeability values of the samples at different frequencies are tabulated in Table S1 in the Supplementary Material.

4. Conclusions

In summary, biphasic lithium iron oxide nanocomposites with different phase fractions of α-$LiFe_5O_8$ and α-$LiFeO_2$ were prepared and their EMI shielding performance in the X-band was studied. Detailed analyses of the crystal structure, morphology, and dielectric and magnetic properties demonstrated that the EMI shielding performance can be tuned by controlling the physical properties as well as the interfaces, with the biphasic samples exhibiting superior performance compared to the single-phase sample. The latter is evident in the chart presented in Fig. 8 where we show a comparison of the mean shielding parameters of the different samples across the X-band. The single-phase sample (S_1: 100 wt% α-Fe_2O_3) is taken as the base sample since it has the poorest shielding performance. The shielding parameters of S_1 have been subtracted from those of S_2, S_3, and S_4 to obtain the difference values. Mean difference values were then computed by taking the average throughout the X-band, which are then plotted as percentage change with respect to the corresponding values for S_1.

The biphasic samples (S_2 and S_3) have higher SE_A values due to greater absorption (with nearly 80 % increase compared to single-phase S_1). Notably, although the percentage increase in SE_A for S_3 is marginally less than that of S_2, S_3 exhibits the maximum improvement in total shielding (SE_T), since it also has a higher reflection (SE_R) than all the other samples. Both reflection and absorption contribute to the shielding performance of S_3. For S_2, the shielding mechanism is completely dominated by absorption, whereas, in the case of S_4 reflection is dominant. From this comparison, it can be concluded that the use of S_2 absorbers is preferred in applications requiring minimizing disturbance to the radiation performance of microwave sensors since the shielding mechanism of S_2 is predominantly absorption-based (SE_A), resulting in low reflection (SE_R). On the other hand, S_3 absorbers are well-suited for applications requiring isolation between multiple microwave sensors as they not only absorb radiation but also reflect microwaves away from the sensors, ensuring optimal isolation [74–77]. Additionally, both S_2 and S_3 offer wide EABs in the X band and can be used as efficient microwave absorbers. This work thus offers fundamental insights for the intelligent design of EMI shielding materials based on specific applications and needs.

CRediT authorship contribution statement

Sagnik Ghosh: Writing – review & editing, Writing – original draft,

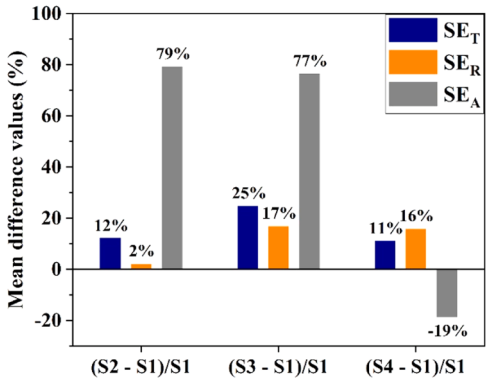

Fig. 8. Mean difference values of shielding parameters of the biphasic samples (in %) with respect to single-phase S_1.

Validation, Investigation, Formal analysis, Conceptualization. **Mustafa Aboulsaad:** Writing – review & editing, Writing – original draft, Validation, Investigation, Formal analysis. **Pramod Rangaiah:** Writing – review & editing, Writing – original draft, Validation, Investigation, Formal analysis. **Gianni Barucca:** Writing – review & editing, Writing – original draft, Validation, Investigation, Formal analysis. **Tomas Edvinsson:** Writing – review & editing. **TAPATI SARKAR:** Writing – review & editing, Writing – original draft, Supervision, Project administration, Funding acquisition, Conceptualization. **Davide Peddis:** Writing – review & editing, Supervision. **Sawssen Slimani:** Writing – review & editing. **Robin Augustine:** Writing – review & editing. **Bagher Aslibeiki:** Formal analysis, Writing – review & editing. **Johan Cedervall:** Writing – review & editing, Writing – original draft, Formal analysis.

Declaration of Competing Interest

The authors declare that they have no known competing financial interests or personal relationships that could have appeared to influence the work reported in this paper.

Acknowledgements

The authors thank Rajesh Kumar Rajagopal for help in measurements and Mauricio Perez for useful discussions. SG and TS gratefully acknowledge funding from the Swedish Research Council (grant number 2021-03675). MA and TE acknowledge funding from the Swedish Research Council (grant number 2023-05244) and the Swedish Energy Agency (grant number P2020-90215). JC gratefully acknowledges funding from ÅForsk Foundation (grant number 22-378).

Appendix A. Supporting information

Supplementary data associated with this article can be found in the online version at doi:10.1016/j.jallcom.2024.177017.

Data Availability

Data will be made available on request.

References

[1] M. Solkin, Electromagnetic interference hazards in flight and the 5G mobile phone: Review of critical issues in aviation security, Transp. Res. Procedia 59 (2021) 310–318, https://doi.org/10.1016/j.trpro.2021.11.123.
[2] R. van der Togt, Electromagnetic interference from radio frequency identification inducing potentially hazardous incidents in critical care medical equipment, JAMA 299 (2008) 2884, https://doi.org/10.1001/jama.299.24.2884.
[3] G. Schmitt, J. Brachmann, B. Waldecker, L. Navarrete, T. Beyer, A. Pfeifer, W. Kubler, Implantable Cardioverter Defibrillator: Possible Hazards of

Electromagnetic Interference, Pacing Clin. Electrophysiol. 14 (1991) 982–984, https://doi.org/10.1111/j.1540-8159.1991.tb04145.x.
[4] J. Paś, S. Duer, Determination of the impact indicators of electromagnetic interferences on computer information systems, Neural Comput. Appl. 23 (2013) 2143–2157, https://doi.org/10.1007/s00521-012-1165-1.
[5] M. Kaur, S. Kakar, D. Mandal, Electromagnetic interference. in: 2011 3rd International Conference on Electronics Computer Technology, IEEE, 2011, pp. 1–5, https://doi.org/10.1109/ICECTECH.2011.5941844.
[6] J. Burrell, Disruptive Effects of Electromagnetic Interference on Communication and Electronic Systems, 2003. ⟨https://citeseerx.ist.psu.edu/document?repid=rep1&type=pdf&doi=5c429bf0b7ec04c0df8b28b73c6c55e7c52e363a⟩ .
[7] S.S. Seker, O. Simsek, Brief review of biological effects of electromagnetic pollution (RF and 5G Waves) on humans, animals, and vegetation, Int. J. Innov. Res. Sci., Eng. Technol. 11 (2023), https://doi.org/10.15680/IJIRSET.2022.1112001.
[8] A. Balmori, Electromagnetic pollution from phone masts. Effects on wildlife, Pathophysiology 16 (2009) 191–199, https://doi.org/10.1016/j.pathophys.2009.01.007.
[9] P. Raju, J. Shankar, J. Anjaiah, C. Kalyani, G. Neeraja Rani, Complex permittivity and permeability properties analysis of NiCuZn Ferrite-Polymer nanocomposites for EMI suppressor applications. in: J Phys Conf Ser, Institute of Physics Publishing, 2020, https://doi.org/10.1088/1742-6596/1495/1/012001.
[10] R.K. Mishra, M.G. Thomas, J. Abraham, K. Joseph, S. Thomas, Electromagnetic Interference Shielding Materials for Aerospace Application. in: Advanced Materials for Electromagnetic Shielding, Wiley, 2018, pp. 327–365, https://doi.org/10.1002/9781119128625.ch15.
[11] M.M. Harussani, S.M. Sapuan, G. Nadeem, T. Rafin, W. Kirubaanand, Recent applications of carbon-based composites in defence industry: a review, Def. Technol. 18 (2022) 1281–1300, https://doi.org/10.1016/j.dt.2022.03.006.
[12] N. Devi, S.S. Ray, Electromagnetic interference cognizance and potential of advanced polymer composites toward electromagnetic interference shielding: a review, Polym. Eng. Sci. 62 (2022) 591–621, https://doi.org/10.1002/pen.25876.
[13] J. Kruželák, A. Kvasničáková, K. Hložeková, I. Hudec, Progress in polymers and polymer composites used as efficient materials for EMI shielding, Nanoscale Adv. 3 (2021) 123–172, https://doi.org/10.1039/d0na00760a.
[14] V. Shukla, Review of electromagnetic interference shielding materials fabricated by iron ingredients, Nanoscale Adv. 1 (2019) 1640–1671, https://doi.org/10.1039/c9na00108e.
[15] S. Varshney, A. Ohlan, V.K. Jain, V.P. Dutta, S.K. Dhawan, In situ synthesis of polypyrrole-γ-Fe_2O_3-Fly ash nanocomposites for protection against EMI pollution, Ind. Eng. Chem. Res 53 (2014) 14282–14290, https://doi.org/10.1021/ie500512d.
[16] R.S. Yadav, I. Kuritka, J. Vilcáková, M. Machovský, D. Škoda, P. Urbánek, M. Masar, M. Goralik, M. Urbánek, L. Kalina, J. Havlica, Polypropylene nanocomposite filled with spinel ferrite $NiFe_2O_4$ nanoparticles and in-situ thermally-reduced graphene oxide for electromagnetic interference shielding application, Nanomaterials 9 (2019), https://doi.org/10.3390/nano9040621.
[17] M. Zahid, S. Siddique, R. Anum, M.F. Shakir, Y. Nawab, Z.A. Rehan, M-Type Barium Hexaferrite-Based Nanocomposites for EMI Shielding Application: a Review, J. Supercond. Nov. Magn. 34 (2021) 1019–1045, https://doi.org/10.1007/s10948-021-05859-1.
[18] K. Bhaskaran, R.K. Bheema, K.C. Etika, The influence of Fe_3O_4@GNP hybrids on enhancing the EMI shielding effectiveness of epoxy composites in the X-band, Synth. Met 265 (2020), https://doi.org/10.1016/j.synthmet.2020.116374.
[19] C. Sun, C. Cheng, M. Sun, Z. Zhang, Facile synthesis and microwave absorbing properties of $LiFeO_2$/$ZnFe_2O_4$ composite, J. Magn. Magn. Mater. 482 (2019) 79–83, https://doi.org/10.1016/j.jmmm.2019.03.034.
[20] J. Li, D. Zhou, P. Wang, W. Liu, J. Su, Raspberry-like LiFe5O8nanoparticles embedded on MoS_2 microflowers with excellent microwave absorption performance, J. Mater. Chem. A Mater. 8 (2020) 20337–20345, https://doi.org/10.1039/d0ta07483g.
[21] Y. Lin, J. Dong, H. Zong, B. Wen, H. Yang, Synthesis, Characterization, and Electromagnetic Wave Absorption Properties of Composites of Reduced Graphene Oxide with Porous $LiFe_5O_8$ Microspheres, ACS Sustain Chem. Eng. 6 (2018) 10011–10020, https://doi.org/10.1021/acssuschemeng.8b01307.
[22] C. Wan, J. Li, Synthesis and electromagnetic interference shielding of cellulose-derived carbon aerogels functionalized with α-Fe_2O_3 and polypyrrole, Carbohydr. Polym. 161 (2017) 158–165, https://doi.org/10.1016/j.carbpol.2017.01.003.
[23] P. Manjappa, H.K. Rajan, M.G. Mahesh, K.G. Sadananda, M. Channegowda, G. Kumar Shivashankar, N.B. Mutt, Effective Attenuation of Electromagnetic Waves by Synergetic Effect of α-Fe2O3 and MWCNT/Graphene in LDPE-Based Composites for EMI Applications, (2022). https://doi.org/10.3390/ma.
[24] J.M.F. Lucas, P.R. Prezas, S. Soreto Teixeira, N.M. Ferreira, A.J.M. Sales, B.M. G. Melo, M.P.F. Graça, Tuning the magnetic and electric behavior of lithium ferrite using an eco-friendly pectin sol-gel route, J. Solgel Sci. Technol. 98 (2021) 580–592, https://doi.org/10.1007/s10971-021-05513-1.
[25] S.S. Teixeira, M.P.F. Graça, L.C. Costa, Dielectric and structural properties of lithium ferrites, Spectrosc. Lett. 47 (2014) 356–362, https://doi.org/10.1080/00387010.2013.840316.
[26] V. Mohanty, G. Govindaraj, $Li_{0.5}Ce_xFe_{2.5-x}O_4$ (x = 0, 0.05): Hydrothermal synthesis, electrical and magnetic properties, Mater. Res Express (5) (2018), https://doi.org/10.1088/2053-1591/aac0cf.
[27] A. Sutka, G. Mezinskis, Sol-gel auto-combustion synthesis of spinel-type ferrite nanomaterials, Front Mater. Sci. 6 (2012) 128–141, https://doi.org/10.1007/s11706-012-0167-3.
[28] A. Kumar, M. Bhatt, N. Yadav, N.K. Mishra, P. Chaudhary, R. Singh, Sol-Gel Derived Nanomaterials and It's Applications: A Review, 2015. ⟨https://www.isca.me/rjcs/Archives/v5/i12/10.ISCA-RJCS-2015-152.pdf⟩.
[29] C. Granados-Miralles, A. Serrano, P. Prieto, J. Guzmán-Mínguez, J.E. Prieto, A. M. Friedel, E. García-Martín, J.F. Fernández, A. Quesada, Quantifying Li-content for compositional tailoring of lithium ferrite ceramics, J. Eur. Ceram. Soc. 43 (2023) 3351–3359, https://doi.org/10.1016/j.jeurceramsoc.2023.02.011.
[30] K. Gong, Y. Peng, A. Liu, S. Qi, H. Qiu, Ultrathin carbon layer coated MXene/PBO nanofiber films for excellent electromagnetic interference shielding and thermal stability, Compos Part A Appl. Sci. Manuf. 176 (2024) 107857, https://doi.org/10.1016/j.compositesa.2023.107857.
[31] H. Zhao, T. Gao, J. Yun, L. Chen, Robust liquid metal reinforced cellulose nanofiber/MXene composite film with Janus structure for electromagnetic interference shielding and electro-/photothermal conversion applications, J. Mater. Sci. Technol. 191 (2024) 23–32, https://doi.org/10.1016/j.jmst.2023.12.035.
[32] Y. Zhang, K. Ruan, K. Zhou, J. Gu, Controlled Distributed $Ti_3C_2T_x$ Hollow Microspheres on Thermally Conductive Polyimide Composite Films for Excellent Electromagnetic Interference Shielding, Adv. Mater. 35 (2023) 2211642, https://doi.org/10.1002/adma.202211642.
[33] C. Wei, L. Shi, M. Li, M. He, M. Li, X. Jing, P. Liu, J. Gu, Hollow engineering of sandwich NC@Co/NC@MnO_2 composites toward strong wideband electromagnetic wave attenuation, J. Mater. Sci. Technol. 175 (2024) 194–203, https://doi.org/10.1016/j.jmst.2023.08.020.
[34] H.M. Rietveld, A profile refinement method for nuclear and magnetic structures, J. Appl. Crystallogr 2 (1969) 65–71, https://doi.org/10.1107/S0021889869006558.
[35] J. Rodríguez-Carvajal, Recent advances in magnetic structure determination by neutron powder diffraction, Phys. B Condens Matter 192 (1993) 55–69, https://doi.org/10.1016/0921-4526(93)90108-I.
[36] S.Y. An, I.B. Shim, C.S. Kim, Synthesis and magnetic properties of $LiFe_5O_8$ powders by a sol-gel process, J. Magn. Magn. Mater. 290-291 (PART 2) (2005) 1551–1554, https://doi.org/10.1016/j.jmmm.2004.11.244.
[37] H. Mansour, H. Letifi, R. Bargougui, S. De Almeida-Didry, B. Negulescu, C. Autret-Lambert, A. Gadri, S. Ammar, Structural, optical, magnetic and electrical properties of hematite (α-Fe_2O_3) nanoparticles synthesized by two methods: polyol and precipitation, Appl. Phys. A Mater. Sci. Process 123 (2017), https://doi.org/10.1007/s00339-017-1408-1.
[38] M.K. Srivastava, U. Kumar, Structural and optical properties of α-Fe_2O_3 nanoparticles realized by simple thermal decomposition route, Phys. Scr. 96 (2021), https://doi.org/10.1088/1402-4896/abc281.
[39] I. Jõgi, T.J. Jacobsson, M. Fondell, T. Wätjen, J.O. Carlsson, M. Boman, T. Edvinsson, Phase formation behavior in ultrathin iron oxide, Langmuir 31 (2015) 12372–12381, https://doi.org/10.1021/acs.langmuir.5b03376.
[40] S. Soreto, M. Graça, M. Valente, L. Costa, Lithium Ferrite: Synthesis, Structural Characterization and Electromagnetic Properties. in: Magnetic Spinels - Synthesis, Properties and Applications, InTech, 2017, https://doi.org/10.5772/67034.
[41] W. Cook, M. Manley, Raman characterization of α- and β-$LiFe_5O_8$ prepared through a solid-state reaction pathway, J. Solid State Chem. 183 (2010) 322–326, https://doi.org/10.1016/j.jssc.2009.11.011.
[42] A.E. Abdel-Ghany, A. Mauger, H. Groult, K. Zaghib, C.M. Julien, Structural properties and electrochemistry of α-$LiFeO_2$, J. Power Sources 197 (2012) 285–291, https://doi.org/10.1016/j.jpowsour.2011.09.054.
[43] Z. An, J. Zhang, S. Pan, G. Song, Novel peanut-like α-Fe_2O_3 superstructures: Oriented aggregation and Ostwald ripening in a one-pot solvothermal process, Powder Technol. 217 (2012) 274–280, https://doi.org/10.1016/j.powtec.2011.10.038.
[44] K. Raja, M. Mary Jaculine, M. Jose, S. Verma, A.A.M. Prince, K. Ilangovan, K. Sethusankar, S. Jerome Das, Sol-gel synthesis and characterization of α-Fe_2O_3 nanoparticles, Superlattices Micro 86 (2015) 306–312, https://doi.org/10.1016/j.spmi.2015.07.044.
[45] B. Vallina, J.D. Rodriguez-Blanco, A.P. Brown, L.G. Benning, J.A. Blanco, Enhanced magnetic coercivity of α-Fe_2O_3 obtained from carbonated 2-line ferrihydrite, J. Nanopart. Res. 16 (2014), https://doi.org/10.1007/s11051-014-2322-5.
[46] M. Tadić, D. Marković, V. Spasojević, V. Kusigerski, M. Remškar, J. Pirnat, Z. Jagličić, Synthesis and magnetic properties of concentrated α-Fe_2O_3 nanoparticles in a silica matrix, J. Alloy. Compd. 441 (2007) 291–296, https://doi.org/10.1016/j.jallcom.2006.09.099.
[47] L. Néel, Magnetism and Local Molecular Field, Science 174 (1979) (1971) 985–992, https://doi.org/10.1126/science.174.4013.985.
[48] M. Dasari, G.R. Gajula, D.H. Rao, A.K. Chintabathini, S. Kurimella, B. Somayajula, Lithium ferrite: The study on magnetic and complex permittivity characteristics, Process. Appl. Ceram. 11 (2017) 7–12, https://doi.org/10.2298/PAC1701007D.
[49] I.F. Waheed, E.T. Bakir, N.A. Dahham, F.G. Saab, R.J. Kadhem, E.T.B. Al-Tikrity, Annealing Temperature Effects on Lithium Ferrite Nanoparticles Structure Prepared by Auto-combustion and Study the Magnetic Properties, 2019. ⟨https://www.researchgate.net/publication/344541688⟩.
[50] P.P. Mohapatra, P. Dobbidi, Effect of carbon reinforcement on the EMI shielding response of $LiFe_5O_8$ ceramics, Mater. Charact. 189 (2022), https://doi.org/10.1016/j.matchar.2022.111985.
[51] J.R. Martínez, J.R. de Alba, I.G. Blanco-Esqueda, A. Guerrero-Serrano, G. Ortega-Zarzosa, Coercivity Values Enhancement by Incorporation of Magnetic Powders in Inorganic Matrix Hosts, N. J. Glass Ceram. 03 (2013) 1–5, https://doi.org/10.4236/njgc.2013.31001.

[52] Xavier BatlleAmílcar Labarta, Finite-size effects in fine particles: magnetic and transport properties, J. Phys. D. Appl. Phys. 35 (2002) 201, https://doi.org/10.1088/0022-3727/35/6/201.
[53] M. Peng, F. Qin, Clarification of basic concepts for electromagnetic interference shielding effectiveness, J. Appl. Phys. 130 (2021), https://doi.org/10.1063/5.0075019.
[54] S. Kim, J.S. Oh, M.G. Kim, W. Jang, M. Wang, Y. Kim, H.W. Seo, Y.C. Kim, J.H. Lee, Y. Lee, J.Do Nam, Electromagnetic interference (EMI) transparent shielding of reduced graphene oxide (RGO) interleaved structure fabricated by electrophoretic deposition, ACS Appl. Mater. Interfaces 6 (2014) 17647–17653, https://doi.org/10.1021/am503893v.
[55] J. Prasad, A.K. Singh, K.K. Haldar, M. Tomar, V. Gupta, K. Singh, $CoFe_2O_4$ nanoparticles decorated MoS_2-reduced graphene oxide nanocomposite for improved microwave absorption and shielding performance, RSC Adv. 9 (2019) 21881–21892, https://doi.org/10.1039/c9ra03465j.
[56] K. Chandra Babu Naidu, S. Roopas Kiran, W. Madhuri, Microwave Processed NiMgZn Ferrites for Electromagnetic Intereference Shielding Applications, IEEE Trans. Magn. 53 (2017), https://doi.org/10.1109/TMAG.2016.2625773.
[57] C. Sun, K.-Y. Zhao, M.-L. Huang, C.-L. Luo, X.-D. Chen, M. Wang, Structure regulating of metal clusters in carbonized metallic organic frameworks for high-efficient microwave absorption via tuning interaction strength between metals and ligands, Nano Res 17 (2024) 1699–1709, https://doi.org/10.1007/s12274-023-6255-0.
[58] M.L. Huang, C.L. Luo, C. Sun, K.Y. Zhao, Y. Ou, M. Wang, Surface structural engineering of carbonyl iron powder for enhancing microwave absorption and anti-oxidation performance, J. Mater. Sci. Technol. 178 (2024) 201–209, https://doi.org/10.1016/j.jmst.2023.08.052.
[59] K.Y. Zhao, C.L. Luo, C. Sun, M.L. Huang, M. Wang, Construction of heterogeneous interfaces on Ti_3AlC_2 micro-particles via surface dotting liquid metal to enhance electromagnetic wave absorption performance, Compos Part A Appl. Sci. Manuf. 173 (2023) 107640, https://doi.org/10.1016/j.compositesa.2023.107640.
[60] C. Sun, K.Y. Zhao, M.L. Huang, C.L. Luo, X.D. Chen, H. Wu, M. Wang, Heterointerface construction for permalloy microparticles through the surface modification of bilayer metallic organic frameworks: Toward microwave absorption enhancement, J. Colloid Interface Sci. 644 (2023) 454–465, https://doi.org/10.1016/j.jcis.2023.04.104.
[61] A.P. Guo, X.J. Zhang, S.W. Wang, J.Q. Zhu, L. Yang, G.S. Wang, Excellent Microwave Absorption and Electromagnetic Interference Shielding Based on Reduced Graphene Oxide@MoS_2/Poly(Vinylidene Fluoride) Composites, Chempluschem 81 (2016) 1305–1311, https://doi.org/10.1002/cplu.201600370.
[62] Y. Wang, H. Guan, C. Dong, X. Xiao, S. Du, Y. Wang, Reduced graphene oxide (RGO)/Mn_3O_4 nanocomposites for dielectric loss properties and electromagnetic interference shielding effectiveness at high frequency, Ceram. Int 42 (2016) 936–942, https://doi.org/10.1016/j.ceramint.2015.09.022.
[63] J. Prasad, A.K. Singh, J. Shah, R.K. Kotnala, K. Singh, Synthesis of MoS2-reduced graphene oxide/Fe_3O_4 nanocomposite for enhanced electromagnetic interference shielding effectiveness, Mater. Res Express 5 (2018), https://doi.org/10.1088/2053-1591/aac0c2.
[64] K. Singh, A. Ohlan, R.K. Kotnala, A.K. Bakhshi, S.K. Dhawan, Dielectric and magnetic properties of conducting ferromagnetic composite of polyaniline with γ-Fe_2O_3 nanoparticles, Mater. Chem. Phys. 112 (2008) 651–658, https://doi.org/10.1016/j.matchemphys.2008.06.026.
[65] M. Praveen, B.P. Harichandra, M. Kumar, R. Harikrishna, G.S. Karthikeya, H.R. Swamy, S. Koul, B.M. Nagabhushana, Zirconium ferrite incorporated Polymer nanocomposite for Electromagnetic wave-absorbing materials in the X-band range, n.d. https://doi.org/https://dx.doi.org/10.2139/ssrn.4751180.
[66] J. Liang, Y. Wang, Y. Huang, Y. Ma, Z. Liu, J. Cai, C. Zhang, H. Gao, Y. Chen, Electromagnetic interference shielding of graphene/epoxy composites, Carbon N. Y 47 (2009) 922–925, https://doi.org/10.1016/j.carbon.2008.12.038.
[67] K. Mabhouti, M. Karamirad, P. Norouzzadeh, M.M. Golzan, R. Naderali, Measurement of electric and magnetic properties of zno nanoparticles in the X-Band Using Nicolson–Ross–Weir analysis, J. Electron Mater. 49 (2020) 3668–3676, https://doi.org/10.1007/s11664-020-08071-4.
[68] C. Singh, S. Bindra Narang, I.S. Hudiara, K. Sudheendran, K.C. James Raju, Complex permittivity and complex permeability of Sr ions substituted Ba ferrite at X-band, J. Magn. Magn. Mater. 320 (2008) 1657–1665, https://doi.org/10.1016/j.jmmm.2007.11.002.
[69] N.N. Jiang, Y. Yang, Y.X. Zhang, J.P. Zhou, P. Liu, C.Y. Deng, Influence of zinc concentration on structure, complex permittivity and permeability of Ni-Zn ferrites at high frequency, J. Magn. Magn. Mater. 401 (2016) 370–377, https://doi.org/10.1016/j.jmmm.2015.10.003.
[70] X. Chang, Z. Duan, D. Wang, S. Wang, Z. Lin, B. Ma, K. Wu, High-Entropy spinel ferrites with broadband wave absorption synthesized by simple solid-phase reaction, Molecules 28 (2023), https://doi.org/10.3390/molecules28083468.
[71] M. Hotta, M. Hayashi, K. Nagata, Complex permittivity and permeability of α-Fe_2O_3 and $Fe_{1-x}O$ powders in the microwave frequency range between 0.2 and 13.5 GHz, ISIJ Int. 50 (2010) 1514–1516, https://doi.org/10.2355/isijinternational.50.1514.
[72] S. Zecchi, G. Cristoforo, M. Bartoli, A. Tagliaferro, D. Torsello, C. Rosso, M. Boccaccio, F. Acerra, A comprehensive review of electromagnetic interference shielding composite materials, Micro (Basel) 15 (2024), https://doi.org/10.3390/mi15020187.
[73] Z. Gao, Z. Jia, J. Zhang, A. Feng, Z. Huang, G. Wu, Tunable microwave absorbing property of La_xFeO_3/C by introducing A-site cation deficiency, J. Mater. Sci.: Mater. Electron. 30 (2019) 13474–13487, https://doi.org/10.1007/s10854-019-01715-0.
[74] P.K.B. Rangaiah, B. Mandal, E. Avetisyan, A.S. Chezhian, B. Augustine, M.D. Perez, R. Augustine, Preliminary Analysis of Burn Degree Using Non-invasive Microwave Spiral Resonator Sensor for Clinical Applications, Front Med Technol. 4 (2022), https://doi.org/10.3389/fmedt.2022.859498.
[75] B. Mandal, A. Chatterjee, P. Rangaiah, M.D. Perez, R. Augustine, A Low Profile Button Antenna with Back Radiation Reduced By FSS. in: 2020 14th European Conference on Antennas and Propagation (EuCAP), IEEE, 2020, pp. 1–5, https://doi.org/10.23919/EuCAP48036.2020.9135328.
[76] P.K.B. Rangaiah, R.L. Karlsson, A.S. Chezhian, L. Joseph, B. Mandal, B. Augustine, M. Mani, M.D. Perez, T. Voigt, R. Augustine, Realization of a portable semi-shielded chamber for evaluation of fat-intrabody communication, IEEE Access 11 (2023) 72743–72755, https://doi.org/10.1109/ACCESS.2023.3289393.
[77] P.K.B. Rangaiah, J. Engstrand, T. Johansson, S. Member, M.D. Perez, R. Augustine, A.K. Pramod, B Rangaiah, 92 Mb/s fat-intrabody communication (Fat-IBC) with low-Cost WLAN hardware, IEEE Trans. Biomed. Eng. 71 (2024) 89, https://doi.org/10.3030/965044.